Effects of Super-Hydrophobic Coatings on Free Falling Spheres

M. Castagna[1]**, M. P. Eisfelder**[2]**, H. Taylor**[2]**, N. Mazellier**[1]**, A. Kourta**[1] **and J. Soria**[2]

[1]PRISME Laboratory
University of Orléans, 45072, Orléans, France

[2]Laboratory for Turbulence Research in Aerospace and Combustion
Department of Mechanical and Aerospace Engineering, Monash University, Melbourne, VIC 3800, Australia

Abstract

The present work deals with a joint experimental investigation of free falling super-hydrophobic spheres in pure water at rest. The results derive from a collaboration between the University of Orléans (France) and the Monash University (Australia). The super-hydrophobic coatings have the ability, once immersed into water, to reduce the contact area between the liquid and the solid surface by entrapping an air layer in the surface roughness. We thus investigate a possible effect of this feature on the hydrodynamic drag of spheres, focusing on the terminal velocity region. Surprisingly, the hydrodynamic performance of super-hydrophobic coatings depends on the analysed Reynolds number regime. The drag increase evidenced for the small diameter spheres tends progressively to turn into a drag attenuation for the largest diameters spheres. A possible connection between the hydrodynamic performance and the deformation of the air layer encapsulating the coated spheres is proposed.

Introduction

Many areas of research over the past centuries originated from the effort to artificially reproduce natural features in order to solve complex problems. This is known in literature as *biomimetics* [20]. Among others, the famous example of the lotus leaf [3] inspired scientists to develop self-cleaning, anti-icing, anti-corrosion and drag reducing super-hydrophobic (SH) surfaces [21]. These properties derive from a combination of surface texturing and chemical repellency [19]. In fact, the physiochemical properties of SH surfaces in the so-called Cassie-Baxter state [4] enable them to entrap a gas layer in their roughness, thus reducing the solid-liquid contact area. This feature could be crucial for the application of SH surfaces in the naval and underwater domains as an alternative of current toxic anti-biofouling methods [7] or as a passive technique for skin friction drag mitigation [18]. In the framework of drag reduction, many experimental and numerical works have demonstrated the beneficial effect of SH surfaces at laboratory scale [17]. However, the extrapolation of these promising results on large-scale realistic applications still represents a tough challenge. Some practical issues such as the stability of the gas/liquid interface [15] or the implementation of expensive SH coating manufacturing procedures [14] need further investigations. In detail, very few works that analysed the effects of SH coatings on macroscopic bluff bodies are available in literature, sometimes reporting contradictory results. McHale et al. [11] performed free falling experiments of SH coated acrylic spheres with and without the encapsulating air layer in a terminal Reynolds number (Re_∞, based on sphere diameter d and terminal falling velocity V_∞) range $1 \times 10^4 \leq Re_\infty \leq 3 \times 10^4$. They reported a $\approx 10\%$ drag decrease in the case of SH spheres in the Cassie-Baxter state. On the contrary, a $\approx 10\%$ terminal velocity decrease was evaluated by Ahmmed et al. [2] in their study on laser-textured polytetrafluoroethylene SH falling spheres at $Re_\infty \approx 5 \times 10^3$. These discordant results show that further efforts need to be accomplished in order to reinforce the

understanding of the flow over macroscopic SH bluff bodies.

In this study we manufactured SH coatings via a spray coating method which is easily implementable on large-scale real applications. We investigated the effect of the surface roughness by embedding micron-sized powders with different nominal particle size. The presented findings result from a joint exploitation of a smaller-size experimental rig located in the University of Orléans (France) and a larger-size experimental set-up situated in Monash University (Australia), which will be described in the following section. The implemented experimental rigs and post-processing techniques allow for a continuous monitoring in time of the falling sphere velocity. However, in this short paper we focus our attention on the terminal velocity region. We will show the effects of the SH coatings on the terminal drag over the whole analysed Re_∞ range. Finally, a possible interaction between the drag variations and the phenomena occurring at the SH sphere surface is discussed.

Experimental Set-up

Experimental Rig

The falling sphere experiments were performed by exploiting two complementary experimental rigs at the University of Orléans (France) and Monash University (Australia). Figure 1 shows a scheme of both the facilities. The falling sphere experimental rig in Orléans consists of a transparent tank with a 100×100 mm^2 square cross-section and a 650 mm height, whilst at Monash it comprises a larger 250×250 mm^2 square cross-section and a 1800 mm height. The results presented in this study are the average of at least ten independent trials for each sphere. A settling time of at least 15 minutes was imposed between two subsequent tests in order to assure the fluid was completely quiescent. All the tests were performed at a room temperature of $19 \pm 1\ °C$. Uncoated magnetic stainless steel spheres with nominal diameters ranging from $d = 5$ to 25 mm were used as reference. An electromagnetic holder was used to gently dip the spheres below the water surface in order to assure a null velocity at release time. The trajectory of the falling sphere was recorded by a Phantom V341 high-speed camera at a 2560×1100 px^2 resolution at Orléans whilst 2 PCO Dimax S4 cameras with a 2016×2016 px^2 resolution were used at Monash. This resulted into a conversion factor of 300 μm/px, with a recording rate of 1000 fps. The presence of a mirror placed at $45°$ with respect to the tank enabled the simultaneous recording of the front and side views with a single camera, thus providing information on the three-dimensional (3D) displacement of the falling sphere. The post-processing of the recorded videos enabled the reconstruction of the 3D displacement of the falling sphere, and was performed with the commercial software MATLAB®. A cross-correlation code was developed to detect the sphere displacement between two consecutive images. A sub-pixel accuracy was reached thanks to the implementation of a Gaussian fit of the correlation peak [16]. The code was validated by generating artificial images describing
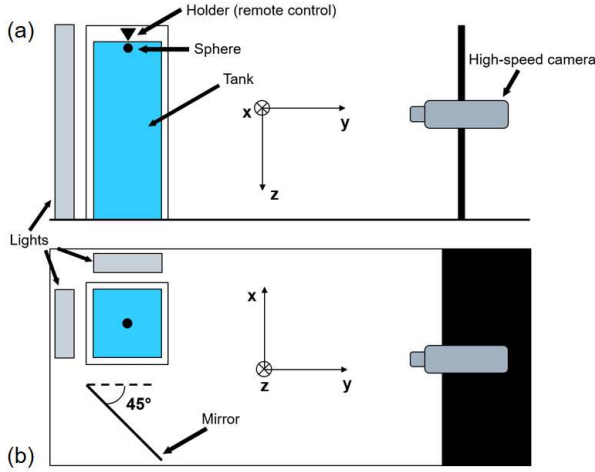
Figure 1: The falling sphere experimental set-up: (a) side view and (b) top view. The scheme describes both the rigs in Orléans (France) and Melbourne (Australia), since they differ only in the tank size.

the vertical motion of a sphere. The accuracy was estimated to be approximately $\pm\,0.06$ px, lower than 0.4% of the smallest investigated diameter. The evaluated terminal velocities were in the range $0.8 - 2.5\ \mathrm{ms^{-1}}$, which correspond to a Reynolds number range $0.5 \times 10^4 - 6.4 \times 10^4$.

Additional tests were performed with a high magnification configuration in order to investigate more closely the phenomena occurring at the SH spheres surface during the fall. In that case, a $2048\times1152\ \mathrm{px^2}$ window was used, with a recording rate of 1300 fps. The spatial resolution increased up to 60 μm/px.

Super-Hydrophobic Coatings

The SH spheres were produced by applying a SH coating over the reference spheres via a spray method, using a commercially available SH painting (Ultra-Ever Dry®). The deposition of carbon-based powders with different nominal particle sizes enabled us to control the macro-scale surface texture. The three produced SH coatings will be indicated hereinafter SH-1, SH-2 and SH-3 in order of increasing root-mean square surface roughness λ values. The latter was evaluated by 3D confocal microscopy measurements over SH flat plates (see figure 2), with values of 25 μm, 74 μm and 142 μm for the SH-1, SH-2 and SH-3 coatings respectively. Contact angle measurements were performed with a digital goniometer via the sessile drop technique. Double-distilled water drops with a volume of 6 μL were deposited over SH horizontal flat plates providing static contact angles θ_s in the range $145° \pm 2° - 161° \pm 3°$. The reported uncertainties represent the 95% confidence level. The highest θ_s was obtained with the SH-1 coating, whilst a λ increase induced a θ_s reduction, in good agreement with the findings reported in [14] for surface roughness in the same range of our study. The same approach was followed to evaluate the roll-off θ_r angle by tilting the SH flat plates at a controlled rate of 0.5 °/s. The θ_r angle, which was considered in this study as the lowest tilt angle that caused the drop to roll-off, reached the highest value of $5.4° \pm 3.2°$ in the SH-3 case, whereas a λ decrease determined a θ_r reduction down to $1.6° \pm 0.2°$ for the SH-1 coating. The SH coatings caused a d increase (measurement accuracy 10 μm) with respect to the reference spheres, with a maximum +10% in the SH-3 case. Finally, the SH coatings induced a mass (measurement accuracy 0.1 mg) increase up to +6% in the SH-3 case.
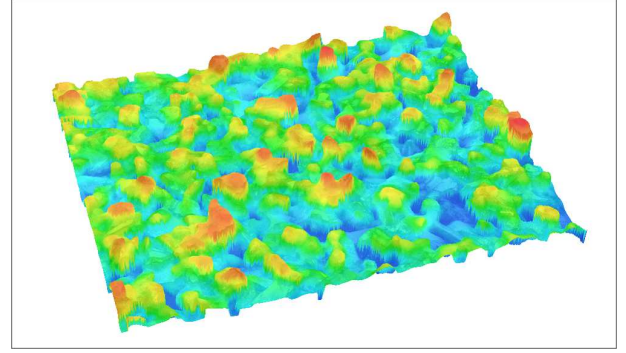

Figure 2: Confocal microscopy analysis of a portion of a flat plated covered with the SH-2 coating. The colour scale (blue-to-red) indicates the surface roughness (0-170 μm). Notice the random spatial distribution of the powder particles.

Full details of the experimental set-up, SH coatings manufacturing procedure, sphere properties and post-processing techniques were presented in [5].

Results and Discussion

Since the transversal motion was one order of magnitude smaller than the corresponding vertical motion, the terminal drag coefficient $C_{D\infty}$ can be evaluated by the following relation [12]:

$$C_{D\infty} = \frac{4dg\,(\zeta - 1)}{3V_\infty^2},\qquad(1)$$

where g is the acceleration due to gravity and $\zeta = \rho_s/\rho_f$, the density ratio between sphere and fluid, was in the range $6.2 - 7.8$. Equation 1 describes the balance between drag and gravity/buoyancy forces once the terminal velocity V_∞ has been reached. The high ζ values justify the predominantly vertical motion of the falling spheres. Figure 3 shows the terminal drag coefficient $C_{D\infty}$ as a function of the terminal Reynolds number Re_∞ for all the analysed spheres, including the results from the Australian experimental rig in the high Re_∞ region. Data obtained by [10] in their review of previous works concerning reference spheres are displayed in figure 3 for assessment purposes. A good agreement between our reference results and the data available in literature, especially in the low Re_∞ region, is noticed. The slight deviation at higher Re_∞ may be due to the fitting procedure of multiple previous work performed by [10].
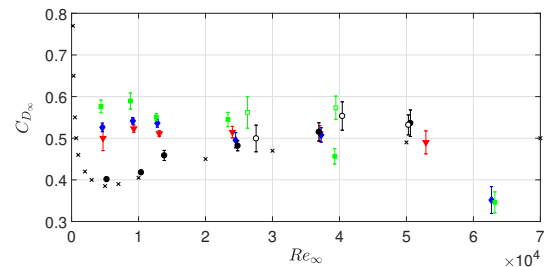

Figure 3: Terminal drag coefficient $C_{D\infty}$ as a function of the terminal Reynolds number Re_∞ for all the investigated spheres. $\bullet$, reference (smooth) sphere. $\blacktriangledown$, SH-1 coating. $\blacklozenge$, SH-2 coating. $\blacksquare$, SH-3 coating. $\times$, reference spheres experimental data from [10]. The empty symbols represent the Monash results, with colors and shapes corresponding to the full symbols. The error bars represent the 95% confidence level.

Concerning the SH coatings, drag increase up to +45% with respect to the corresponding reference sphere is found in the low Re_∞ region. Moreover, the increase of the surface roughness λ of the SH coatings translates into a more pronounced drag augmentation. This trend is not followed for increasing Re_∞. In fact, the increase in sphere diameter induces a gradual attenuation of the drag increase of the SH spheres. A switch of the behaviour is noticed between the $d = 15$ mm and $d = 20$ mm spheres ($Re_\infty \approx 3 \times 10^4$), leading to a drag decrease due to the SH coatings in the largest Re_∞ region analysed. A drag decrease down to -35% is evaluated for the SH-3 coating at $Re_\infty \approx 6.4 \times 10^4$. The partial available Australian results seem to confirm the gradual attenuation of the drag increase, even if happening at higher Re_∞. The drag variation $\Delta C_D = \left(C_{D\infty}^{SH} - C_{D\infty}^{ref} \right) / C_{D\infty}^{ref}$ due to SH coatings with respect to the reference spheres is even more evident in figure 4. The approximately linear behaviour of the drag variation with respect to the non-dimensional surface roughness is highlighted by the linear fit indicated by the dashed lines. The experimental data follow the linear law:

$$\Delta C_D = \alpha_D \frac{\lambda}{d} + \Delta C_{D0}, \tag{2}$$

where the slope α_D strongly depends on the analysed sphere diameter. The change of sign of α_D between $d = 15$ mm and $d = 20$ mm underlines the different influence on drag of SH coatings in the different Re_∞ regions.
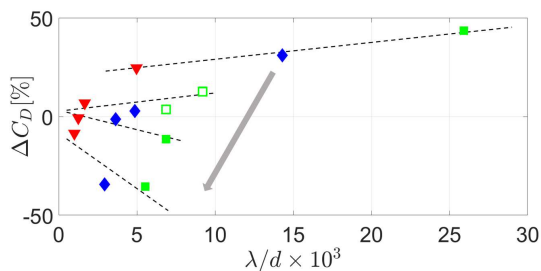
Figure 4: Terminal drag coefficient variation with respect to the reference sphere as a function of the non-dimensional roughness. ▼, SH-1 coating. ◆, SH-2 coating. ■, SH-3 coating, □, SH-3 coating Monash University. The dashed lines highlight the linear behaviour (see equation 2). The grey arrow indicates increasing sphere diameter d. For the sake of readability, only results for $d = 5$, 15, 20 and 25 mm are reported.

A closer look at the phenomena occurring at the SH falling spheres' surface seemed to be necessary in order to try to explain the evidenced terminal drag variations. Figure 5 shows two snapshots taken during the fall of two SH-3 coated spheres. These images clearly show that the air layer encapsulating the SH spheres is far from being motionless and non-deformable. The assumptions made in various analytical and numerical analyses [8] thus seem not to be able to catch the complex phenomena happening at the SH surface, at least under the investigated operating conditions. Macroscopic protrusions are noticed at the back-side of the falling spheres, both in figure 5(a) and 5(b). While a single protrusion covering the whole rear-side is found in the small diameter spheres case (figure 5(a)), multiple spots are seen for increasing sphere diameter (figure 5(b)). Interestingly, the typical height of these air protrusions remains approximately constant (≈ 1.5 mm) despite varying the sphere diameter and thus, the Re_∞ region. The influence of the deformed air layer could therefore be more pronounced at the smallest analysed diameters, since the global shape tends to be spherical at
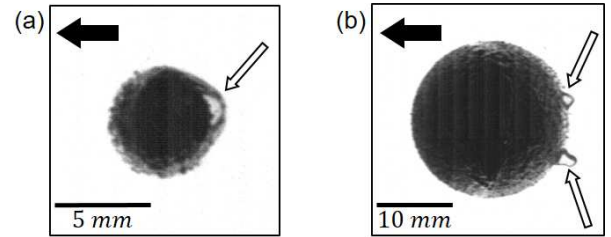
Figure 5: Typical images recorded during the fall of a SH-3 sphere using the high magnification configuration. (a) $d = 5$ mm, (b) $d = 20$ mm. The black arrows denote the gravity direction. The white arrows indicate the region where the air deformation is visible.

the largest diameters. This behaviour is recorded with all the analysed SH coatings.

Figure 6 shows a time sequence recorded in the high magnification configuration for the $d = 5$ mm, SH-3 coated sphere. This sequence lets us observe an interesting peculiarity of the air protrusion, which is not detectable from the analysis of a single snapshot. In fact, the image sequence clearly demonstrates that the air protrusion, while getting deformed, moves around the back-side of the falling sphere. This is evident from the images where an air protrusion is no more unambiguously detectable. This suggests a possible interaction between the air layer and the flow surrounding the bluff body. In detail, the air protrusion is evident in the region that undergoes separation of the laminar boundary layer, typical of the so-called sub-critical regime [1] which characterises all the performed tests. This lets us speculate that the pressure jump caused by the flow separation could promote the partial suction of the air entrapped in the surface roughness. The air layer compliance and dynamics could therefore be intimately connected to the wake developing behind the falling sphere. If that is the case, a possible feedback of the air layer movement and deformation on the flow is likely to occur. Figure 7 presents this interaction: the unsteady pressure gradient induced by the separation of the laminar boundary layer around the sphere promotes the motion and the deformation of the air layer encapsulating the sphere. This translates into a non-negligible modification of the boundary condition at the sphere wall, which in turn could modify the production of vorticity at the wall and the intensity of vorticity released in the wake [13]. This in turn can impact the pressure gradient, closing the loop.

Conclusions

In this joint experimental work, free falling super-hydrophobic sphere tests were carried out. The coatings were produced via a spray manufacturing procedure suitable for real large-scale applications. The surface roughness was varied by embedding micron-sized powders with different nominal particle size. The influence of the SH coatings on the terminal drag was analysed. The drag increase evidenced in the low Reynolds number region tends to progressively turn into a drag mitigation at the highest Reynolds numbers investigated. A possible connection between the drag variations and the deformation of the air layer which encapsulates the super-hydrophobic spheres is investigated. Finally, a mechanism involving an interplay between the flow characteristics, the air layer deformation and the vorticity production at the wall is proposed. Further examination of the influence of these SH coatings on spheres and how the flow field is influenced would provide coupling between the near and far-field effects.
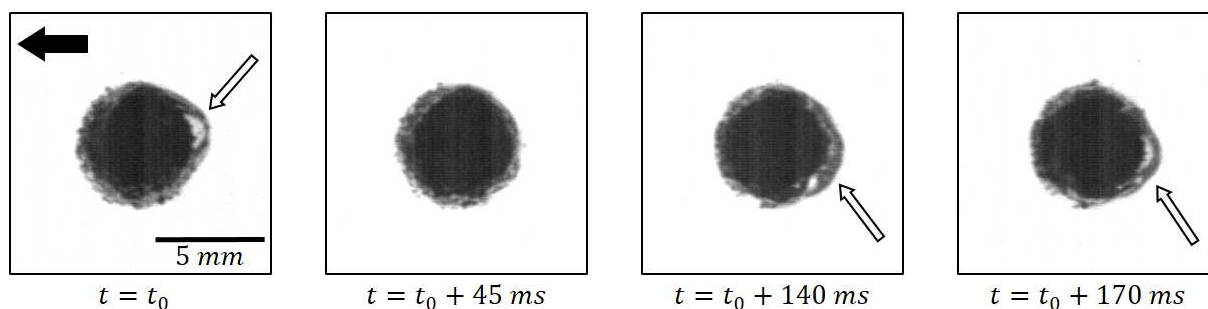
Figure 6: Typical snapshots recorded in high magnification configuration illustrating the movement and deformation of the air layer (indicated by white arrows) around SH-3 coated spheres. The black arrow represent the gravity direction. The variable t_0 designates a randomly chosen time origin.
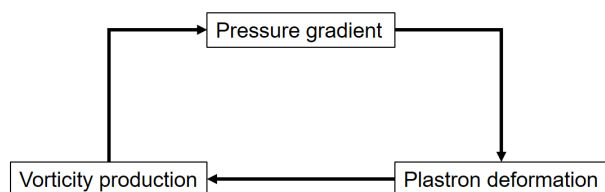

Figure 7: A possible driving mechanism of the mutual interaction between the flow and the air layer.

References

[1] Achenbach, E., Experiments on the flow past spheres at very high Reynolds numbers *J. Fluid Mech.*, **54**, 1972, 565–575.

[2] Ahmmed, K. M. T., Patience, C. and Kietzig, A.-M., Internal and External Flow over Laser-Textured Superhydrophobic Polytetrafluoroethylene (PTFE) *ACS Appl. Mater. Interfaces*, **8**, 2016, 27411–27419.

[3] Barthlott, W. and Neinhuis, C., Purity of the sacred lotus, or escape from contamination in biological surfaces *Planta*, **202**, 1997, 1–8.

[4] Cassie, A. B. D. and Baxter, S., wettability of porous surfaces, *Trans. Faraday Soc.*, **40**, 1944, 546–551.

[5] Castagna, M., Mazellier, N. and Kourta, A., Wake of super-hydrophobic falling spheres: influence of the air layer deformation, *J. Fluid Mech.*, **850**, 2018, 646–673.

[6] Epps, B. P., Truscott, T. T. and Techet, A. H., in *Proceedings of Mathematical Methods in Engineering International Symposium, MMEI, Coimbra, Portugal*, 54–57.

[7] Genzer, J. and Efimenko, K., Recent developments in superhydrophobic surfaces and their relevance to marine fouling: a review, *Biofouling*, **22(5)**, 2006, 339–360.

[8] Gruncell, B. R. K., Sandham, N. D. and McHale, G., Simulations of laminar flow past a superhydrophobic sphere with drag reduction and separation delay, *Phys. Fluids*, **25**, 2013, 043601.

[9] Jenny, M., Dušek, J. and Bouchet, G., Instabilities and transition of a sphere falling or ascending freely in a Newtonian fluid, *J. Fluid Mech.*, **508**, 2004, 201–239.

[10] Lapple, C. E, and Sheperd, C. B., Calculation of particle trajectories, *Ind. Eng. Chem.*, **32**, 1940, 605–617.

[11] McHale, G., Shirtcliffe, N. J., Evans, C. R. and Newton, M.-I., Terminal velocity and drag reduction measurements on superhydrophobic spheres, *Appl. Phys. Lett.*, **94**, 2009, 064104.

[12] Mordant, M. and Pinton, J.-F., Velocity measurement of a settling sphere, *Eur. Phys. J. B*, **18**, 2000, 343–352.

[13] Mougin, G. and Magnaudet, J., Path instability of a rising bubble, *Phys. Rev. Lett.*, **88(1)**, 2002, 014502.

[14] Nilsson, M. A., Daniello, R. J. and Rothstein, J. P., A novel and inexpensive technique for creating superhydrophobic surfaces using Teflon and sandpaper, *J. Phys. D: Appl. Phys.*, **43**, 2010, 1–5.

[15] Piao, L. and Park, H., Two-Dimensional Analysis of Air-Water Interface on Superhydrophobic Grooves under Fluctuating Water Pressure, *Langmuir*, **31**, 2015, 8022–8032.

[16] Raffel, M., Willert, C., Wereley, S. and Kompenhans, J., Particle Image Velocimetry, Springer, 2007.

[17] Rothstein, J. P., Slip on superhydrophobic surfaces, *Annu. Rev. Fluid Mech.*, **42**, 2010, 89–109.

[18] Samaha, M. A., Tafreshi, H. V. and Gad-el-Hak, M., Superhydrophobic surfaces: from the lotus leaf to the submarine, *C. R. Mecanique*, **340**, 2012, 18–34.

[19] Shirtcliffe, N. J., McHale, G., Atherton, S. and Newton, M. I., An introduction to superhydrophobicity, *Adv. Colloid Interface Sci.*, **161**, 2010, 124–138.

[20] Vincent, J. F. V., Bogatyreva, O. A., Bogatyrev, N. R., Bowyer, A. and Pahl, A.-K., Biomimetics: its practice and theory, *J. R. Soc. Interface*, **3**, 2006, 471–482.

[21] Zhang, X., Shi, F., Niu, J., Jiang, Y. and Wang, Z., Superhydrophobic surfaces: from structural control to functional application, *J. Mater. Chem*, **18**, 2008, 621–633.